Central Lancashire Online Knowledge (CLoK)

Title	Magnetic fields in the close neighborhood of LDN 328 core
Type	Article
URL	https://knowledge.lancashire.ac.uk/id/eprint/57553/
DOI	https://doi.org/10.1093/mnras/staf2061
Date	2026
Citation	Gupta, Shivani, Soam, Archana, Karoly, Janik and Lee, Chang Won (2026) Magnetic fields in the close neighborhood of LDN 328 core. Monthly Notices of the Royal Astronomical Society, 545 (4). ISSN 0035-8711
Creators	Gupta, Shivani, Soam, Archana, Karoly, Janik and Lee, Chang Won

Magnetic fields in the close neighbourhood of LDN 328 core

Shivani Gupta [1,2]⋆ Archana Soam,[1] Janik Karoly[3] and Chang Won Lee[4,5]

[1]*Indian Institute of Astrophysics, II Block, Koramangala, Bengaluru 560034, India*
[2]*Pondicherry University, R.V. Nagar, Kalapet, Puducherry 605014, India*
[3]*Department of Physics and Astronomy, University College London, London WC1E 6BT, UK*
[4]*Korea Astronomy and Space Science Institute (KASI), 776 Daedeokdae-ro, Yuseong-gu, Daejeon 34055, Korea*
[5]*University of Science and Technology (UST), 217 Gajeong-ro, Yuseong-gu, Daejeon 34113, Korea*

ABSTRACT

Linearly polarized dust emission traces the plane-of-sky magnetic field structure, thus allowing us to investigate the role of magnetic fields in the formation and evolution of cloud cores. In this work, we present observations of dust polarization at 850 µm wavelength towards the LDN 328 (hereafter L328) core and its neighbourhood regions, classified as R1, R2, and R3, using the James Clerk Maxwell Telescope (JCMT) with SCUBA-2 (Submillimetre Common User Bolometer Array 2)/POL-2. This study extends our previous work on magnetic fields in L328 across different spatial scales. We used the JCMT/POL-2 data in the near vicinity of the L328 core to study the magnetic fields in its nearby regions. We identified clumps in these regions using the 'FellWalker' algorithm and derived the dust temperature and column density by fitting the spectral energy distribution using combined JCMT and *Herschel* dust continuum maps. We analysed the magnetic field morphology in the vicinity of the L328 core and employed the structure function analysis to determine the magnetic field dispersion angle. We used the modified Davis–Chandrasekhar–Fermi method to estimate magnetic field strengths and also derived the mass-to-flux ratio and Alfvén Mach number.

Key words: polarization – ISM: clouds – dust, extinction – ISM: magnetic fields – submillimetre: ISM.

1 INTRODUCTION

In the current understanding of star formation, clumps within molecular clouds serve as the precursors to dense cores and, ultimately, to formed stars (C. J. Lada & E. A. Lada 2003). These clumps, typically larger structures with hydrogen volume densities of $n(H_2) > 10^2$–10^4 cm^{-3}, are expected to fragment into smaller, denser cores as they evolve (T. V. Veltchev, S. Donkov & R. S. Klessen 2013). This fragmentation is influenced by a combination of turbulence, gravity, thermal pressure, and magnetic fields (*B*-fields), determining whether these clumps will efficiently collapse into star-forming cores (P. Hennebelle & G. Chabrier 2008; P. Hennebelle & S.-i. Inutsuka 2019; K. Pattle et al. 2023). However, not all clumps necessarily evolve into gravitationally bound cores or active star-forming regions. Some remain quiescent, while others may disperse before forming stars. Understanding the physical conditions, stability, and fragmentation properties of clumps is therefore crucial to constraining the initial conditions of star formation (M. R. Bate, I. A. Bonnell & V. Bromm 2003). While the relative importance of *B*-fields versus turbulence remains debated, their role in clump evolution and star formation efficiency is critical (A. Soam et al. 2024).

Submillimetre (submm) observations are an essential tool for tracing high-extinction (A_V) regions, as cooler dust grains emit thermal radiation, allowing us to trace the denser parts of the cloud, such as clumps or cores. Since clumps are primarily composed of dust and gas, their structures are best studied at submm wavelengths, where their *B*-fields can be analysed through polarization measurements. The plane-of-the-sky *B*-field (B_{pos}) is measured by linear polarization of light by aligned dust grains (J. S. Hall 1949; W. A. Hiltner 1949). So far, the radiative torque (RAT) alignment is the most accepted mechanism explaining the dust grain alignment in the interstellar medium (A. Z. Dolginov & I. G. Mitrofanov 1976; A. Lazarian & T. Hoang 2007; T. Hoang & A. Lazarian 2008; B. G. Andersson, A. Lazarian & J. E. Vaillancourt 2015). The minor axes of the dust grains align with the ambient *B*-field. At longer wavelengths (far-infrared to mm), the *B*-field orientation is inferred by rotating the polarization angle by 90° as thermal dust emission is polarized along the grains' major axes that are perpendicular to the *B*-field.

In this work, we investigate the morphology and strength of the *B*-field in the nearest neighbourhood of the L328 core using the James Clerk Maxwell Telescope (JCMT) 850 µm dust polarization data. Two pre-stellar cores and a low-mass star are found to be forming within the L328 core (see C. W. Lee et al. 2018, for more details). Earlier studies have analysed the *B*-field morphology in L328 using *Planck*, optical, near-infrared, and submm (JCMT) polarization data (A. Soam et al. 2015a, b; Planck Collaboration I 2016b; Planck Collaboration XXVI 2016c; S. Kumar, A. Soam & N. Roy 2023; S. Gupta et al. 2025). The connection of *B*-fields across different wavelengths and spatial scales is illustrated in S. Gupta et al. (2025). To understand the surrounding regions of

this core, we identified the dense, clumpy structures and estimated their temperature, column density, and volume density. Further, we analysed the *B*-field structures in these clumps using our submm polarization measurements.

The structure of the paper is as follows. In Section 2, we present the observations and data reduction. Section 3 elaborates the analysis, results, and discussion. Finally, we summarize our results in Section 4.

2 OBSERVATIONS AND DATA REDUCTION

The observations at 850 µm were conducted with the Submillimetre Common User Bolometer Array 2 (SCUBA-2)/POL-2 on the JCMT in 2018 March (M18AP033; PI: Archana Soam) and in 2019 May and June (M19AP014; PI: Chang Won Lee). The weather conditions during observations were split between $\tau_{225} < 0.05$ and $0.05 < \tau_{225} < 0.08$, where τ_{225} is the atmospheric opacity at 225 GHz. The data were collected using the daisy-map mode (W. S. Holland et al. 2013), specifically optimized for POL-2 observations (P. Friberg et al. 2016). The total integration time for a single field was ∼31 min, with a total of 17 repeats, resulting in an on-source integration time of ≈8.8 h. This work focuses exclusively on the 850 µm data. Further details of the observations and data reduction can be found in S. Gupta et al. (2025).

A polarization vector catalogue was created from the final Stokes *I*, *Q*, and *U* maps by binning up from the 4 arcsec pixel size to 12 arcsec, which approximates the beam size 14.1 arcsec. This process reduces the number of vectors by combining vectors within each 12 arcsec pixel and also decreases the noise level. Specifically, for plotting, we selected vectors with an intensity-to-error ratio $(I/\delta I) > 10$ and a polarization-to-error ratio $2 < (P/\delta P) < 25$.

In order to convert the native map units of pW (picowatt) to astronomical units, a flux calibration factor of 495 Jy beam^{-1} pW^{-1} was used (S. Mairs et al. 2021), multiplied by a factor of 1.35 to account for POL-2 being inserted into the beam. The peak values of total and polarized intensities are found to be ∼100 and ∼11 mJy beam^{-1}, respectively. The rms noise of the background region in the Stokes *I*, *Q*, and *U* maps is measured to be ∼6.26, 5.27, and 5.75 mJy beam^{-1}, respectively. These values were determined by selecting a region about 1 arcmin from the centre of each corresponding map, where the signal remained relatively constant.

The values for the debiased degree of polarization *P* were calculated using the modified asymptotic estimator (S. Plaszczynski et al. 2014; L. Montier et al. 2015):

$$P = \frac{1}{I}[PI - 0.5\sigma^2(1 - e^{-(PI/\sigma)^2}/PI], \tag{1}$$

where *I*, *Q*, and *U* are the Stokes parameters, and $\sigma^2 = (Q^2\sigma_Q^2 + U^2\sigma_U^2)/(Q^2 + U^2)$, where δQ and δU are the uncertainties for Stokes *Q* and *U*.

The polarization position angles θ, measured from north through east on the plane of the sky, were calculated using the relation

$$\theta = \frac{1}{2}\tan^{-1}\frac{U}{Q}, \tag{2}$$

and the corresponding uncertainties in θ were calculated using

$$\delta\theta = \frac{1}{2}\frac{\sqrt{Q^2\delta U^2 + U^2\delta Q^2}}{(Q^2 + U^2)}. \tag{3}$$

The plane-of-sky orientation of the *B*-field is inferred by rotating the polarization angles by 90°.

2.1 Ancillary data

In our analyses, we have adopted the optical (*R* band) polarization data with a polarization-to-error ratio of $(P/\delta P) > 2$ from A. Soam et al. (2013) that was observed using the ARIES (Aryabhatta Research Institute of Observational Sciences) Imaging Polarimeter mounted at the Cassegrain focus of the 104-cm Sampurnanand Telescope, India. We have also used the *Herschel* dust continuum maps to derive the H_2 column density and dust temperature maps for this region (see Section 3.2 for details).

3 RESULT AND DISCUSSION

In Fig. 1, the left panel shows a Digitized Sky Survey (DSS) red continuum-subtracted H α image containing two dark nebulae, L328 (centre, shown with black dashed box) and L331 (upper one). The right panel provides a zoomed-in dust continuum map of the black-box region at 850 µm observations obtained with the JCMT. The white line segments show the *B*-field morphology obtained with POL-2 observations. This whole region is divided into four subregions: R1, R2, R3, and the L328 core. These regions are more distinctly outlined and identified in Fig. 2 with zoomed-in *B*-field structures. Notably, regions R2 and R3 seem to be interconnected by a dusty bridge-like structure. Given their proximity to L328, we assume that regions R1, R2, and R3 are at the same distance of 270 pc as that of the L328 core.

3.1 Dusty structures

Fig. 3 presents the identified clumps overlaid with ellipses, as detected by the FellWalker algorithm.

3.1.1 Clump finding using FellWalker

The FellWalker algorithm (D. S. Berry 2015) was used to identify the clumps in the 850 µm dust continuum image. This algorithm is part of the CUPID package (D. S. Berry et al. 2007) in the STARLINK software.[1] A total of 14 clumps were identified in the observed region (see Fig. 3). In running this algorithm, a source with a peak intensity higher than $3\sigma_{rms}$ and a size larger than the beam size of 14.1 arcsec is identified as a real clump. Pixels with intensities greater than $1.2\sigma_{rms}$ are allowed to be associated with a peak. Two neighbouring peaks are considered separate if the dip between the peaks is larger than $1\sigma_{rms}$ deep. The σ_{rms} value was adopted from S. Gupta et al. (2025). Ellipses were fitted to each clump based on the 30 per cent intensity contour level around its peak intensity, and their corresponding major and minor axes ($\theta_{maj.}$ and $\theta_{min.}$, respectively) as well as position angles (θ_{PA}) were derived to determine their sizes and orientations. θ_{PA} is measured from north towards east on the plane of the sky.

The radius of each detected clump was estimated by considering the deconvolved major and minor axes of the fitted ellipse. The observed major axis ($\theta_{maj.}$) and minor axis ($\theta_{min.}$) include contributions from the beam size (14.1 arcsec). To obtain the intrinsic clump size, we subtract the beam contribution and compute the geometric mean
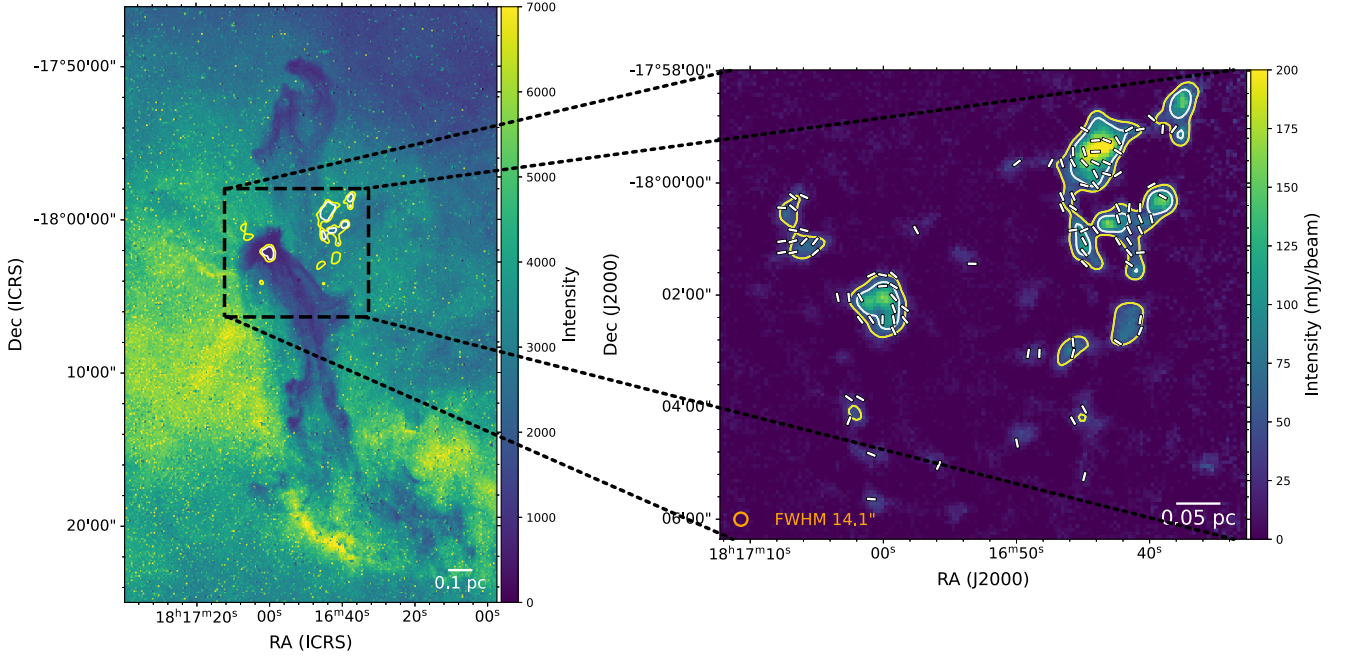
---

[1] https://starlink.eao.hawaii.edu/

Figure 1. Left: DSS red continuum-subtracted H α image of the L328 and L331 regions. Right: 850 μm dust continuum map overlaid with *B*-field vectors obtained from SCUBA-2/POL-2, with the orange circle indicating the beam size. The dotted lines outline the zoomed region. Scale bars are shown in the bottom right of both panels. The yellow contour is at 35 Jy beam^{-1}, and the white contour is at 70 Jy beam^{-1}, taken from the 850 μm continuum image in both images.
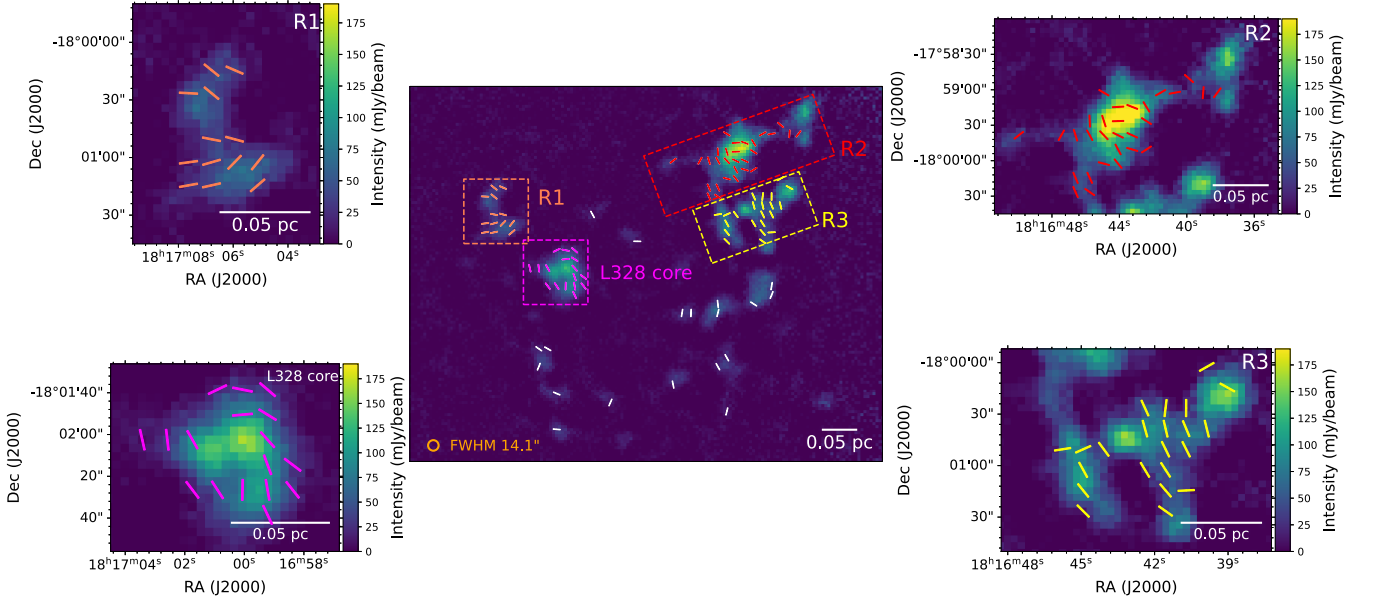

Figure 2. The central panel shows the SCUBA-2/POL-2 850 μm dust continuum map overlaid with *B*-field vectors, highlighting the regions R1, R2, R3, and the L328 core as introduced in the text. The surrounding panels show the individual zoomed-in images of these regions with *B*-field vectors overlaid. The scale bar is shown at the bottom left of each image.

of the deconvolved axes. The final expression for the clump radius is given by

$$R = \sqrt{\frac{\left(\sqrt{\theta_{\text{maj.}}^2 - 14.1^2}\right) \times \left(\sqrt{\theta_{\text{min.}}^2 - 14.1^2}\right)}{4}}. \quad (4)$$

Table 1 summarizes various physical properties of identified clumps.

3.1.2 Matching of clumps with SIMBAD data base

We cross-matched the identified clumps with the help of the SIMBAD data base[2] and found association with the young stellar objects (YSOs) and submillimetre (smm) sources (see Fig. 3 and Table 1). Clumps C1, C2, and C3 are also identified as smm sources: HIGALBM G013.0357−00.7211 (D. Elia et al.
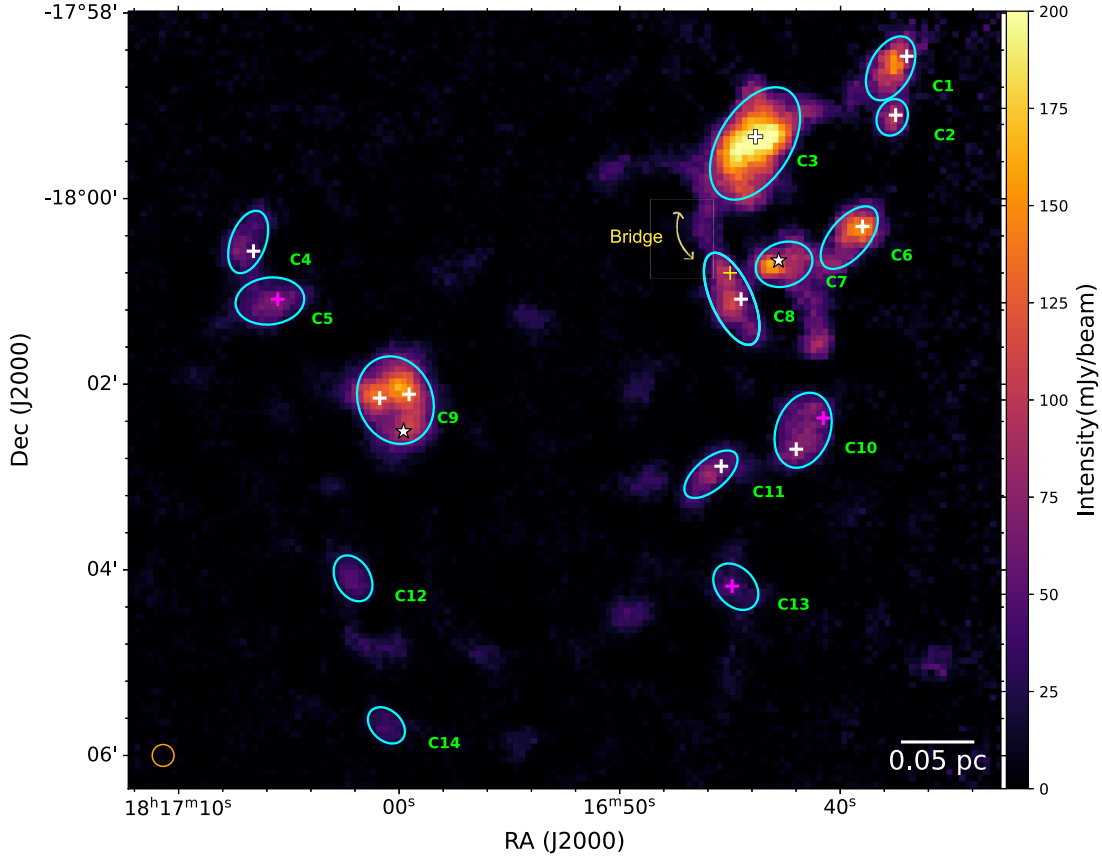
Figure 3. Clumps identified using the FellWalker algorithm are shown as ellipses overlaid on the 850 μm continuum image. The clump numbering follows a right-to-left order. Submm sources are marked with '+', and YSO sources are indicated with '∗'.

2017), SCOPE G013.06−00.73 (D. J. Eden et al. 2019), and AGAL G013.034−00.749 (J. S. Urquhart et al. 2018), respectively. For AGAL G013.034−00.749, the dust temperature is 12.8 K, and the column density $N(H_2)$ is 22.482 (in log scale).

The line width of $C^{18}O$ (2–1) is 0.68 km s^{-1}, the line width of ^{13}CO (2–1) is 1.55 km s^{-1}, and the optical depth of 1 (J. S. Urquhart et al. 2018).

Clumps C4 and C5 are also identified as smm source named SCOPE G013.06−00.84 (D. J. Eden et al. 2019) and HIGBAL G013.0510−00.8413 (D. Elia et al. 2017), respectively.

Clumps C6, C7, and C8 are associated with SCOPE G013.01−00.74 (D. J. Eden et al. 2019), AGAL G013.011−00.757, which is classified as a YSO (J. S. Urquhart et al. 2018), and SCOPE G013.01−00.77 as well as JCMTLSP J181644.9−180049 (D. J. Eden et al. 2017), respectively. For AGAL G013.034−00.757, the dust temperature is 13.6 K, and the column density $N(H_2)$ is 22.355 (in log scale). The line width of $C^{18}O$ (2–1) is 1.94 km s^{-1}, the line width of ^{13}CO (2–1) is 1.60 km s^{-1}, and the optical depth is 0.46 (J. S. Urquhart et al. 2018).

Clump C9 corresponds to the L328 core, which is having S1 (smm), S2 (YSO), and S3 (smm) subcores (J. Wu et al. 2007). Clump C10 has two smm sources: SCOPE G012.98−00.77 and HIGALBM G012.9856−00.7651. Clumps C11 and C13 are also identified as smm sources as SCOPE G012.99−00.78 and HIGALBM G012.9670−00.7940, respectively.

3.2 Column densities and dust temperatures

This region was observed by the *Herschel Space Observatory* with Photodetector Array Camera and Spectrometer (PACS) at 100 and 160 μm and with Spectral and Photometric Imaging Receiver (SPIRE) at 250, 350, and 500 μm. We use these archival *Herschel* data, combined with our JCMT data at 850 μm, to fit a modified blackbody function (see equation 5) for the dust emission. The *Herschel*/PACS, *Herschel*/SPIRE, and JCMT 850 μm images were smoothed to the SPIRE 500 μm full width at half-maximum beam size of 35.2 arcsec (because it is the maximum beam size) and then reprojected on a common grid (4 arcsec, same as JCMT 850 μm image). The SPIRE data we obtained from the archive have been zero-point corrected using *Planck* data, while such corrections have not been made for the PACS data. We applied an offset correction to the PACS data by adding the background flux level to restore the missing large-scale emission. The spectral energy distribution (SED) for each pixel was fitted assuming the following formula for a modified blackbody emission (see J. Kauffmann et al. 2008):

$$S_\nu = B_\nu(T_d)\left(1 - e^{-\tau_\nu}\right), \tag{5}$$

where

$$B_\nu(T_d) = \frac{2h\nu^3}{c^2}\frac{1}{e^{\frac{h\nu}{k_B T_d}} - 1}, \tag{6}$$

$$\tau_\nu = \mu_{H_2} m_H k_\nu N(H_2), \tag{7}$$

and

$$k_\nu = k_0\left(\frac{\nu}{\nu_0}\right)^\beta, \tag{8}$$

Table 1. Ellipse parameters, including sexagesimal coordinates of centroid positions, major and minor axes, position angles, radius, peak intensity values, dust temperature, column density, volume density, classification of source, and SIMBAD identification (see Section 3.1.2 for references).

Clump ID	RA (h:m:s)	Dec. (°:′:″)	$\theta_{maj.}$ (arcsec)	$\theta_{min.}$ (arcsec)	Aspect ratio	θ_{PA} (°)	Radius (arcsec)	Radius (pc)	I_{peak}, 850 μm (mJy beam⁻¹)	T_{dust} (K)	$N(H_2)$ (×10²¹ cm⁻²)	$n(H_2)$ (×10⁴ cm⁻³)	Type
C1	18:16:37.7	−17:58:35.8	44.75	27.01	1.66	151.39	15.64	0.020	152.2	12.6±0.4	6.7±1.2	5.43±0.97	smm
C2	18:16:37.7	−17:59:07.4	24.35	19.50	1.25	157.15	8.18	0.010	102.6	12.8±0.4	5.8±1.0	9.40±1.62	smm
C3	18:16:43.9	−17:59:24.4	80.57	46.75	1.72	148.00	29.73	0.039	230.4	12.3±0.4	9.2±1.7	3.82±0.71	smm
C4	18:17:06.8	−18:00:28.1	42.15	22.79	1.85	159.94	13.33	0.018	68.8	13.7±0.3	4.0±0.6	3.60±0.54	smm
C5	18:17:05.9	−18:01:06.2	44.54	30.31	1.47	96.29	16.83	0.022	72.2	13.4±0.3	4.6±0.7	3.39±0.52	smm
C6	18:16:39.6	−18:00:25.2	48.75	25.16	1.94	139.44	15.59	0.020	162.2	12.8±0.4	6.3±1.1	5.11±0.89	smm
C7	18:16:42.6	−18:00:42.5	37.46	28.38	1.32	108.40	14.62	0.019	164.0	12.5±0.4	7.7±1.4	6.57±1.19	YSO
C8	18:16:44.9	−18:01:04.8	64.20	26.61	2.41	24.35	18.80	0.025	113.9	13.0±0.3	5.7±0.9	3.69±0.58	2 smm
C9	18:17:00.2	−18:02:10.3	76.2	66.6	1.15	23.30	34.91	0.036	167.3	13.2±0.3	4.9±0.7	2.41±0.32	2 smm and 1 YSO
C10	18:16:41.7	−18:02:29.8	50.06	34.84	1.44	159.88	19.56	0.025	77.7	13.0±0.4	5.7±0.9	3.50±0.58	2 smm
C11	18:16:45.9	−18:02:58.2	41.58	20.02	2.08	129.79	11.79	0.015	87.4	13.3±0.4	4.9±0.7	5.29±0.76	smm
C12	18:17:02.1	−18:04:05.5	31.75	22.36	1.42	30.26	11.11	0.015	48.9	13.8±0.3	3.5±0.5	3.78±0.54	–
C13	18:16:44.7	−18:04:10.9	33.97	24.39	1.39	42.32	12.40	0.016	47.7	13.3±0.4	4.8±0.7	4.86±0.71	smm
C14	18:17:00.6	−18:05:40.6	27.33	19.38	1.41	46.54	8.82	0.012	41.5	14.2±0.3	2.9±0.4	3.92±0.54	–

where S_ν is the measured flux at the observed frequency ν, $B_\nu(T_d)$ is the Planck function for a dust temperature T_d, τ_ν is the optical depth, μ_{H_2} is the mean molecular weight of the hydrogen gas in the cloud, m_H is the mass of a hydrogen atom, $N(H_2)$ is the column density, and κ_ν is the dust opacity (absorption coefficient). We use a value of 2.8 for μ_{H_2}, and κ_ν was calculated for each frequency observed using equation (8), where β is the emissivity spectral index of the dust, and we assume $\kappa_0 = 0.1$ cm² g⁻¹ and $\nu_0 = 10^{12}$ Hz (S. V. W. Beckwith et al. 1990).

The SED fitting for each pixel was done by fixing β as 1.8, while the dust temperature T_d and the column density $N(H_2)$ were fitted simultaneously using the curve_fit function. The resulting temperature and column density maps obtained through this procedure are shown in Fig. 4.

The identified clumps are overplotted on the dust temperature map and column density map, as shown in Fig. 4. The average dust temperature T_d and average column density $N(H_2)$ for each clump are listed in Table 1. The uncertainties in T_d and $N(H_2)$ are estimated from the diagonal elements of the covariance matrix obtained during the SED fitting. For clump C3, the average T_d is 12.3 K, which is consistent with the previously determined value of 12.8 K (J. S. Urquhart et al. 2018). The average $N(H_2)$ is 9×10^{21} cm⁻², which is three times lower than the value of 30×10^{21} cm⁻² reported by J. S. Urquhart et al. (2018). For the L328 core, the average T_d is 13.2 K, which is fairly consistent with the 11.5 K reported by S. Gupta et al. (2025). This discrepancy may be attributed to the offset correction applied to the 100 and 160 μm images prior to the SED fitting.

3.3 Magnetic field morphology

3.3.1 B-fields in clumps

To evaluate whether the *B*-fields within the clumps are aligned or perpendicular to their major axis, we compute the relative angle between the position angle of the clump (θ_{PA}) and the *B*-field orientation ($\theta_{B_{pos}}$), defined as

$$|\theta_{relative}| = \left|\theta_{B_{pos}} - \theta_{PA}\right|. \qquad (9)$$

The right panel of Fig. 5 shows the 850 μm dust continuum map observed by SCUBA-2/POL-2, illustrating the relative orientation ($\theta_{relative}$) of the position of *B*-field ($\theta_{B_{pos}}$) with respect to the clump (θ_{PA}). The colour scale, ranging from 0° to 180°, highlights the relative alignment between the *B*-fields and the clump major axes. The values close to 0° or 180° indicate the parallel alignment, while values near 90° show perpendicular alignment. The parallel configuration suggests that the *B*-fields may facilitate the channelling of material along the major axis of the clump, helping in elongation and subsequent fragmentation (Planck Collaboration XXXV 2016a). The perpendicular configuration may suggest that magnetic pressure is playing a role in resisting gravitational collapse, under the assumption that matter is flowing through the major axis of the clump (P. Hennebelle & S.-i. Inutsuka 2019).

For clumps C1 and C2, there are no *B*-field vectors to analyse. Clump C3 exhibits a mix of all colours, from blue to red, showing a random nature. This may hint at a dynamically active region. In clump C4, the dominance of green colour suggests a perpendicular *B*-field orientation relative to the major axis. Conversely, clump C5 shows the dominance of blue and red colours, indicating parallel alignment. Clump C6 displays colour from blue to red, indicative of a random distribution, which can be due to a limited number of *B*-field vectors. Clump C7 is dominated by green shades, sug-
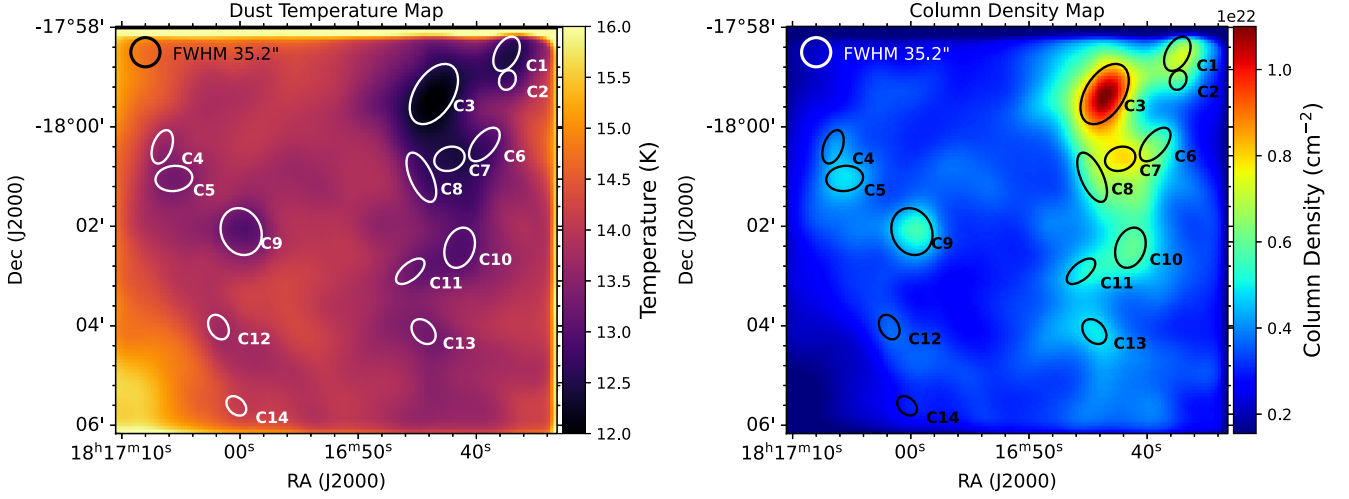
Figure 4. The left panel shows the fitted dust temperature T_d map, and the right panel shows the corresponding column density $N(H_2)$ map. The overlaid ellipses on both plots are the clumps from the SCUBA-2 850 μm dust emission map. Each map is smoothed to the 35.2 arcsec beam size of the *Herschel* 500 μm observations, which is shown by the circle in the upper left corner.
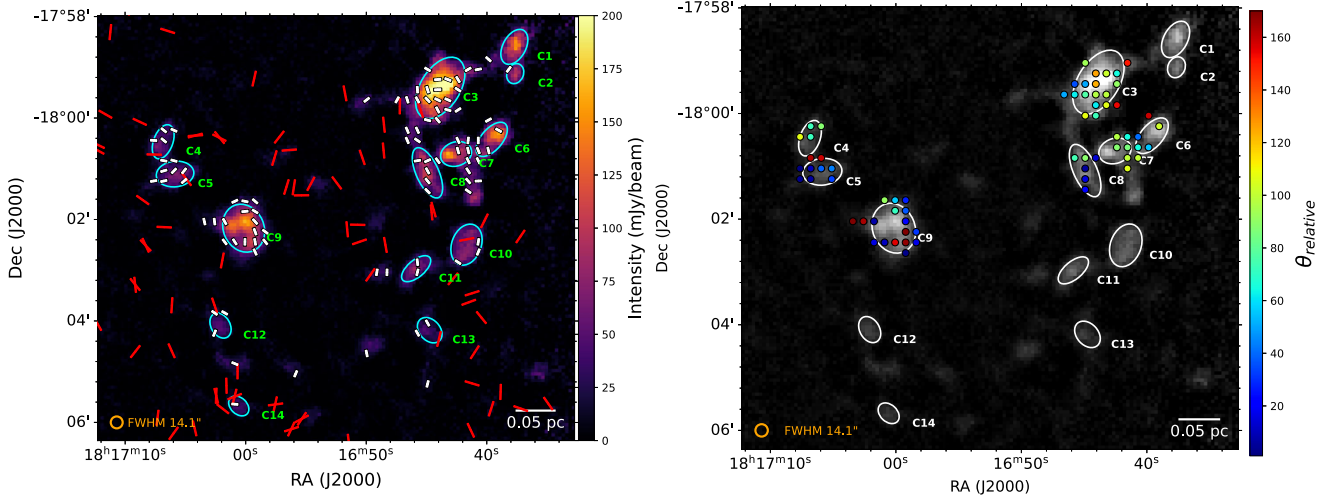

Figure 5. Left: 850 μm dust continuum map overplotted with *B*-field vectors from SCUBA-2/POL-2 (white) and optical observations (red), with the orange circle indicating the beam size. Right: The SCUBA-2/POL-2 850 μm dust continuum map is overplotted with colour-coded circles representing the relative angle between the clump's major axis and the mean *B*-field orientation. The colour scale spans from 0° (blue) to 180° (red). The orange circle at the bottom left indicates the beam size, and the scale bar at the bottom right.

gesting perpendicular alignment. The presence of a YSO within C7 suggests that gravitational collapse is occurring. Clumps C8 and C9 are dominated by blue and red shades, pointing to a preferential parallel alignment. These clumps also show evidence of fragmentation, which may be facilitated by flows along the clump axes. Finally, clumps C10–C14 lack a sufficient number of *B*-field vectors and were therefore excluded from further analysis.

For the statistical analysis, we first computed the mean *B*-field position angles for each clump, which are derived by fitting a Gaussian to the histograms of position angles of *B*-field, and their values are listed in the fourth column of Table 2. From these, we calculated the mean $\theta_{relative}$, which is presented in the fifth column of Table 2. The distribution of $\theta_{relative}$ is consistent with the qualitative trends discussed above, confirming the inferred alignment between the *B*-fields and the clump major axes.

3.3.2 B-fields at different scales

The left panel of Fig. 5 illustrates that the *B*-fields at parsec (pc) scales, as seen in optical measurements (red-coloured vectors) and on subparsec scales observed in JCMT measurements (white-coloured vectors). The red vector appears to show more randomness compared to the white ones. This suggests that *B*-fields are getting more uniform on subparsec scales.

Fig. 6 presents dust emission maps at different wavelengths obtained from *Herschel* data archive. At 100 μm, the emission is dominated by hotter dust. As we move to 160, 250, 350, and 500 μm, the emission reveals a colder dust, and we start to see the cloud structures. We noticed that dust structure in general seems to follow a spherical shell morphology. There is a hint of this shell-like structure present in 100 and 850 μm too.

The large-scale *B*-fields mapped with *Planck* in orange-coloured vectors are plotted on all the subplots. The *B*-fields on these scales

Table 2. Aspect ratios, position angles, mean *B*-field orientations, and relative angles for the clumps. The final column indicates whether the *B*-fields are preferentially parallel (∥), perpendicular (⊥), or randomly oriented with respect to the clump major axis.

Clump ID	Aspect ratio	θ_{PA} (°)	$\theta_{B_{pos}}$ (°)	$\theta_{relative}$ (°)	Alignment
C3	1.72	148.00	51.9 ± 34.2	96.1 ± 34.2	Random
C4	1.85	159.94	58.5 ± 3.7	101.4 ± 3.7	⊥
C5	1.47	96.29	113.0 ± 21.6	16.7 ± 21.6	∥
C6	1.94	139.44	24.9 ± 32.3	114.5 ± 32.3	Random
C7	1.32	108.40	20.7 ± 8.9	87.7 ± 8.9	⊥
C8	2.41	24.35	35.1 ± 5.7	10.8 ± 5.7	∥
C9	1.15	23.30	32.6 ± 22.6	9.3 ± 22.6	∥

Figure 6. Dust emission maps at 100 and 160 μm from *Herschel*/PACS, and at 250, 350, and 500 μm from *Herschel*/SPIRE data archives. The 850 μm map is from JCMT/SCUBA-2 observations in this work. All maps are overplotted with white-coloured *B*-field vectors obtained from the SCUBA-2/POL-2. In addition to this, all maps are also overplotted with orange-coloured vectors showing *Planck* polarization. The white circle in the bottom left of each panel indicates the beam size.

Figure 7. The left panel shows the degree of polarization versus the position angle of the *B*-field for regions R2, R3, and the L328 core. The right panel presents Gaussian-fitted histograms of the *B*-field position angles with their mean and standard deviation.

are quite uniform, and the *B*-fields revealed using 850 μm (in white-coloured vectors) are clearly seen to be present in longer wavelengths (i.e. 250–850 μm) maps. In region R1 and L328 core, the *Planck* map shows a magnetic field orientation of approximately 45°, whereas in regions R2 and R3, it tends closer to 30°. This consistent large-scale orientation reflects *Planck*'s sensitivity to grains exposed to the diffuse interstellar radiation field, which extends across large scales but is less sensitive to dense regions. In contrast, the white-coloured *B*-field vectors at 850 μm trace *B*-fields associated with denser regions that may be influenced by local radiation sources. Overlaid on each wavelength map, almost all of these vectors are found to be within the spherical shell seen in *Herschel* emission, demonstrating that the *B*-field is closely associated with the denser regions. This multiwavelength analysis underscores the connection between *B*-field orientation and dust continuum properties across different environments. However, detailed analysis of the shell structure is outside the scope of this paper.

3.3.3 B-fields in different regions

In region R1, the *B*-field has already been defined in terms of two clumps, C4 and C5, in the previous subsection. Region R2 exhibits random field structure, as we can see in Fig. 5, and statistically confirmed in Fig. 7 (upper-right panel), with a large dispersion (σ) of 39.5°. Regions R2 and R3 seem to be connected by a bridge-like diffuse continuum structure at 850 μm, and the field lines seem to follow that bridge.

In region R3, we see that *B*-field lines more or less maintain a consistent orientation. The mean *B*-field orientation in this region is 28°, which may be aligned with the large-scale fields (∼30°). This may suggest a coherent magnetic structure from parsec to subparsec scales. The *B*-field morphology in the L328 core has already been defined in S. Gupta et al. (2025).

The mean polarization *P* (per cent) in regions R1, R2, R3, and L328 core is 11 ± 4 per cent, 9 ± 3 per cent, 10 ± 3 per cent, and 7 ± 3 per cent, respectively. In Fig. 7, we examine the relationship between the degree of polarization *P* (per cent) and the *B*-field orientation represented by $\theta_{B_{pos}}$. The left column shows that region R2 shows most of the *P* values concentrated between position angles 0° and 100°. R3 and L328 core shows most of the *P* values concentrated between position angles 0° and 50°. This suggests that most of the dust grains are aligned along the dominant component of the magnetic field, which is around 50°. The panels in the right column show the Gaussian-fitted histogramic representation of the peak *B*-field orientations in all the regions.

3.4 Magnetic field strength

The plane-of-sky *B*-field strength (B_{pos}) is estimated using the Davis–Chandrasekhar–Fermi (DCF; L. Davis 1951; S. Chandrasekhar & E. Fermi 1953) relation. The DCF method assumes that small-scale turbulent gas motions distort *B*-field lines, and this distortion is related to the Alfvén Mach number of the gas. Generally, polarization angle dispersion is used to estimate this effect. The *B*-field strength (B_0) is estimated using the classic DCF relation:

$$B_0 = \frac{\sqrt{4\pi\rho}\,\sigma_v}{\delta\theta}, \tag{10}$$

where $\rho = \mu_g n_{H_2} m_H$ is the mass density, σ_v is the velocity dispersion, and $\delta\theta$ is the polarization angle dispersion. However, when $\delta\theta$ exceeds ∼25°, the assumption of a weakly perturbed field becomes invalid, potentially leading to underestimated field strengths. The estimated B_{pos} is thus corrected by a factor *Q*, known as the modified DCF relation (R. M. Crutcher et al. 2004), such that

$$B_{pos} = Q B_0, \tag{11}$$

where *Q* is taken to be 0.5, based on studies using synthetic polarization maps generated from numerically simulated clouds (E. C. Ostriker, J. M. Stone & C. F. Gammie 2001), which suggests that the *B*-field strength is uncertain by a factor of 2.

The *B*-field strength calculation is based on three parameters: volume density $n(H_2)$, velocity dispersion σ_v (see Section 3.4.1), and polarization angle dispersion $\delta\theta$ (see Section 3.4.2).

3.4.1 Parameters for B-field estimation

We estimate the volume density of each elliptical clump using the formula

$$n(H_2) = \frac{N(H_2)}{2R}. \tag{12}$$

The average volume density and its uncertainty for each clump are listed in Table 1. The error has been propagated based on the uncertainty in the $N(H_2)$. For region R2, we compute the volume-weighted average density of clumps C1, C2, and C3, which results in a value of $(4.09 \pm 0.60) \times 10^4$ cm^{-3}. For region R3, the volume-weighted average density of clumps C6, C7, and C8 is $(4.71 \pm 0.46) \times 10^4$ cm^{-3}.

In region R2, C3 is the largest clump and captures the majority of polarization vectors. Since C3 is associated with AGAL G013.034−00.749, we adopt a $C^{18}O$ (2–1) line width of 0.68 km s^{-1}. In region R3, we assume the same line width of 0.68 km s^{-1}.

To estimate the polarization angle dispersion, we fitted a Gaussian function to the histogram of $\theta_{B_{pos}}$, as shown in Fig. 7. For region R3, the dispersion $\theta_{B_{pos}}$ is 18.7°, while for region R2, it is 45.6°. Since region R2 exhibits a significantly high dispersion, we employed structure function (SF) analysis (R. H. Hildebrand et al. 2009) to determine $\delta\theta$, which provides a better way to quantify the *B*-field fluctuations.

3.4.2 Structure function analysis

In the SF analysis (R. H. Hildebrand et al. 2009), the *B*-field is assumed to consist of a large-scale structured field, B_0, and a turbulent component, δB. The SF method separates the turbulent component from the large-scale structured field by examining how the dispersion in position angles changes as a function of vector separation l. At some scales larger than the turbulent scale δ, δB should reach its maximum value. At scales smaller than the scale d (above which B_0 varies), the higher order terms of the Taylor expansion of B_0 can be cancelled out. When the separation l is $\delta < l < d$, the SF follows the form

$$\left\langle \Delta\Phi_{tot}^2(l) \right\rangle \approx b^2 + m^2 l^2 + \sigma_M^2(l). \tag{13}$$

In this equation, $\Delta\Phi_{tot}^2(l)$ is the square of the total measured dispersion function, which consists of a constant turbulent contribution (b^2), the contribution from the large-scale structured field ($m^2 l^2$), and the contribution of the measured uncertainty in θ is $\sigma_M^2(l)$. The ratio of the turbulent to the large-scale component of the *B*-field is given by

$$\frac{\delta B}{B_0} = \left(\frac{b^2}{2 - b^2} \right)^{1/2}. \tag{14}$$

Using this ratio, we estimated the *B*-field strength B_0, which is derived from the modified DCF relation incorporating the SF approach:

$$B_0 = \frac{\sqrt{(2 - b^2)\, 4\pi\rho}\, \sigma_v}{b}. \tag{15}$$

Note that the units of b in equation (15) are in radians. We fitted the quadratic model of the angular dispersion function, as given in equation (13), to the dispersion of polarization angle differences in region R2 as a function of the distance between pairs of polarization angles, as shown in Fig. 8. The fitted b values are found to be 24.81° ± 1.54° (0.43 ± 0.03 rad) in region R2. In this region, the B_{pos} is estimated to be 83.4 ± 10.3 μG calculated using equation (15).

In region R1, the clump C4 and C5 have B_{pos} 143.1 ± 17.4 μG and 23.8 ± 2.9 μG, respectively. Note that B_{pos} for C4 is quite high compared to the other three regions. This may be attributed to a lesser number of *B*-field vectors within these clumps that leads to smaller dispersion, resulting in potential overestimation of B_{pos}. For region R3, we determine $\delta\theta$ using the standard deviation of the measured polarization angles, which is 18.7° ± 2.3°, and the mean of observed errors is 8.8°. The calculated $\delta\theta$ is 16.5° (see equation 8 of S. Gupta et al. 2025). The corresponding B_{pos}, calculated from equation (11), is 83.3 ± 15.7 μG.
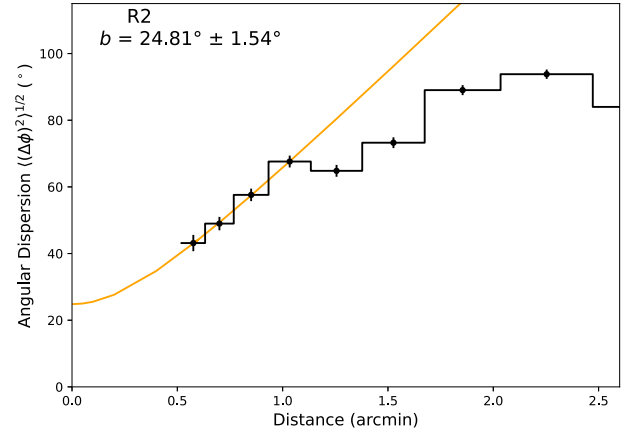

Figure 8. Angular dispersion function of R2 region with angle dispersion segments are shown with black solid circles. The best fit is shown with an orange line.

3.5 Mass-to-flux ratio

Now that we have *B*-field strength for regions R2 and R3, we can test the relative importance of *B*-fields over gravity by calculating the mass-to-flux ratio (λ), as defined by R. M. Crutcher (2004):

$$\lambda = 7.6 \times 10^{-21} \frac{N(H_2)/\text{cm}^{-2}}{B_{pos}/\mu G}. \tag{16}$$

The parameter λ quantifies the balance between magnetic support and gravitational collapse within a structure. When $\lambda < 1$, the structure is considered to be 'magnetically subcritical', suggesting that the structure is supported against gravitational collapse by *B*-fields. In contrast, when $\lambda > 1$, the *B*-field is insufficient to prevent gravitational collapse, thus making the structure 'magnetically supercritical'.

The average column density $N(H_2)$ and its uncertainty for each clump are listed in Table 1. The error has been propagated based on the uncertainty in the $N(H_2)$. For region R1, the values of λ for clump C4 and C5 are 0.2 ± 0.04 and 1.5 ± 0.3, respectively. For region R2, we compute the column-weighted average density of clumps C1, C2, and C3, which results in a value of $(8.54 \pm 1.30) \times 10^{21}$ cm^{-2}. For region R3, the value is $(6.39 \pm 0.63) \times 10^{21}$ cm^{-2}. The value of λ for regions R2 and R3 comes out to be 0.78 ± 0.15 and 0.58 ± 0.12, respectively, suggesting both regions are magnetically subcritical. The L328 core is found to be magnetically transcritical with a λ value of 1.1 ± 0.2 (S. Gupta et al. 2025).

3.6 Alfvén Mach number

The Alfvén Mach number ($\mathcal{M}_A$) quantifies the relative significance of non-thermal motions with respect to the magnetic field. It is defined as the ratio of the non-thermal (turbulent) velocity dispersion (σ_{NT}) to the Alfvén velocity (V_A) as defined by R. M. Crutcher et al. (1999):

$$\mathcal{M}_A = \frac{\sigma_{NT}}{V_A}, \tag{17}$$

where V_A is expressed as

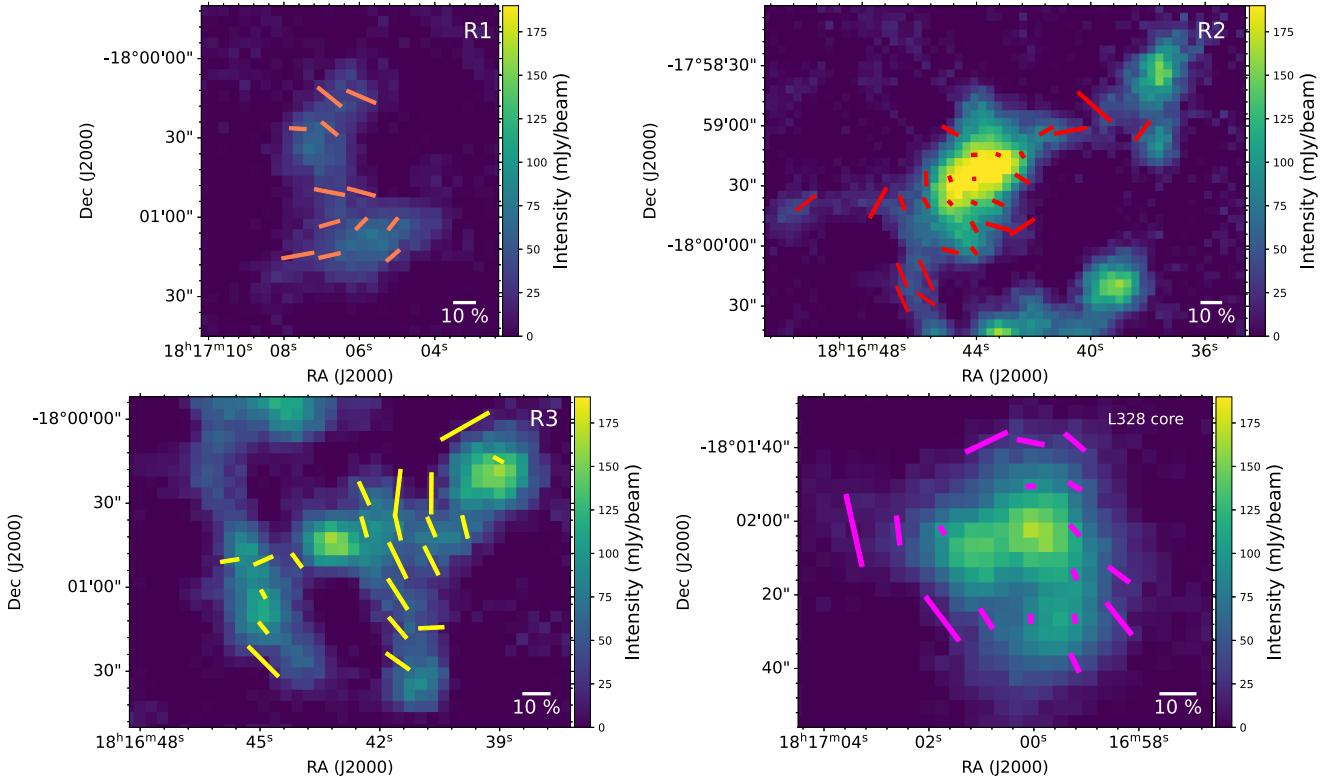$$V_A = \frac{B_{pos}}{\sqrt{4\pi\rho}}. \tag{18}$$

Figure 9. All four regions, R1, R2, R3, and L328 core, are shown with polarization vectors, where the length of the vectors indicates the polarization percentage. A polarization scale bar of 10 per cent is included in each panel for reference.

In region R1, the clumps C4 and C5 exhibit $\mathcal{M}_A$ of 0.26 ± 0.04 and 1.51 ± 0.22, respectively. For regions R2 and R3, the corresponding $\mathcal{M}_A$ values are 0.54 ± 0.08 and 0.58 ± 0.11, while the L328 region shows $\mathcal{M}_A = 0.71 \pm 0.14$. Values of $\mathcal{M}_A < 1$ correspond to sub-Alfvénic regimes, where magnetic fields dominate, $\mathcal{M}_A \approx 1$ indicates a trans-Alfvénic state, where turbulence and magnetic forces are comparable, and $\mathcal{M}_A > 1$ suggests a super-Alfvénic (turbulence-dominated) environment.

Accordingly, clump C4 represents a strongly magnetically dominated region ($\mathcal{M}_A = 0.26$), whereas C5 ($\mathcal{M}_A = 1.51$) is turbulence-dominated. However, these values could partly result from uncertainties in B_{pos} due to the limited number of polarization vectors within the clump. Regions R2, R3, and L328, with $\mathcal{M}_A$ values 0.5–0.7, lie in the sub-Alfvénic regime, implying that magnetic fields dominate over turbulence. Overall, the predominantly sub-Alfvénic nature of these regions (except C5 clump) indicates that magnetic fields dominate over turbulence, thereby delaying the onset of star formation.

3.7 Polarization as a function of intensities

Fig. 9 shows the four regions with overplotted polarization vectors of varying lengths. We observed that the length of the polarization vectors decreases as we move from lower intensity to higher intensity parts in all the regions. Since the length of the vectors corresponds to the polarization fraction, and intensity has a one-to-one correspondence with density, this indicates a drop in polarization fraction toward higher density regimes. This effect is consistently observed across all four regions, as seen in the figure.

This phenomenon, also known as 'depolarization' or 'polarization hole', can be quantitatively analysed by comparing the degree of polarization (P) with total intensity (I) using the relation $P \propto I^{-\alpha}$, as shown in Fig. 10. All four panels in the figure demonstrate a negative correlation between P and I, with slopes $\alpha = 0.97 \pm 0.14$, 0.94 ± 0.07, 0.91 ± 0.14, and 0.98 ± 0.08 for the regions R1, R2, R3, and the L328 core, respectively.

Fig. 11 shows the polarization fraction (P) plotted against intensity (I) for all four regions (R1, R2, R3, and L328) combined. A clear negative correlation between P and I is observed, which follows a power-law relation $P \propto I^{-\alpha}$, with a slope of $\alpha = 0.91 \pm 0.06$. This consistent trend across all regions suggests a similar behaviour of polarization fraction as a function of intensity, irrespective of local variations in physical conditions such as density, B-fields, and turbulence. The combined data improve the robustness of the statistical fit, demonstrating the universality of the relationship between P and I across these regions.

There are several accepted explanations for the observed 'depolarization' effect in starless and star-forming cores. One possible reason is the change in the B-field orientation in denser regions. In denser regions, randomization of gas due to gas–grain collisions can disrupt the alignment of dust grains, reducing alignment efficiency and leading to lower polarization (A. Lazarian 2007; A. Soam et al. 2021). Another possible explanation is magnetic reconnection, where B-field lines break and reconnect, disrupting the uniformity of the field. It can be because of magnetic tangling, also. Since dust grains align with the local B-field, this disruption can reduce their alignment efficiency (A. Lazarian & E. T. Vishniac 1999). Additionally, insufficient radiation causing weak RAT (A. Lazarian & T. Hoang 2007) is another explanation for depolarization.
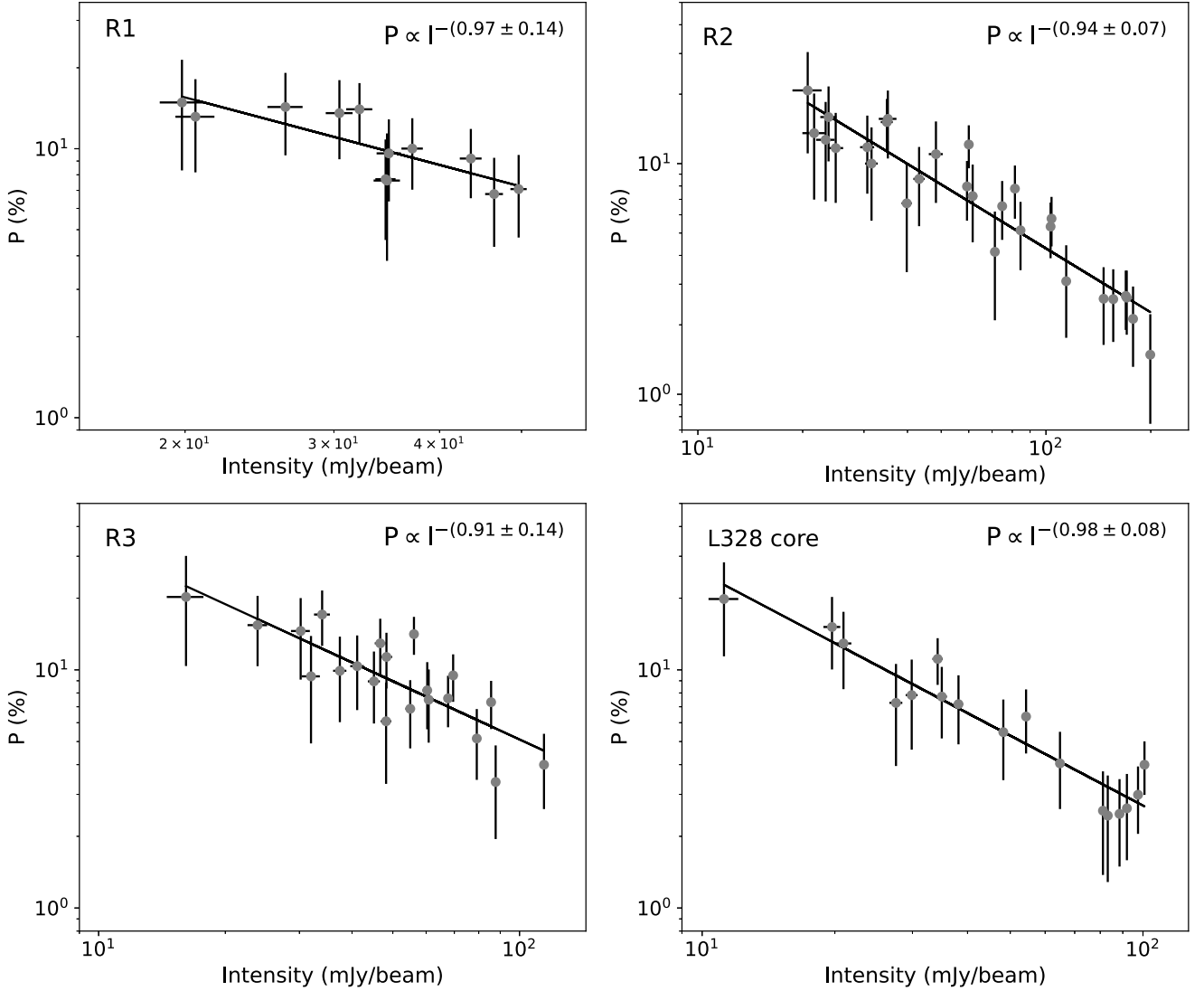
Figure 10. Polarization fraction (P) as a function of intensity in the regions R1, R2, R3, and L328 core regions. The data points represent values and uncertainties based on POL-2 measurements. The fitted lines show the relationship $P \propto I^{-\alpha}$, with the corresponding α values indicated in each panel.
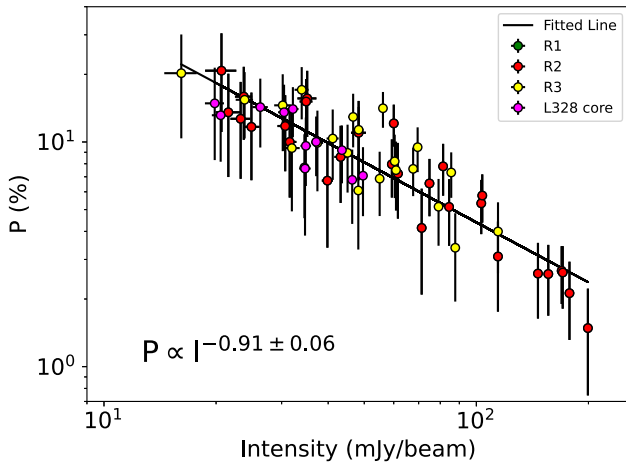

Figure 11. Polarization fraction variation with intensity in the regions R1, R2, R3, and L328 core, based on values and uncertainties from POL-2 measurements.

4 SUMMARY

The paper presents an observational study of the L328 core and its nearby clumps by using $850\,\mu\text{m}$ JCMT/POL-2 dust polarization data. The L328 core and its nearby clumps are divided into four regions for further analysis. The key findings are summarized as follows:

(i) We have identified 14 clumps using the FellWalker algorithm and derived their centroid position, position angle, and radius.

(ii) We estimated the gas column density and the dust temperature of the mapped region by supplementing our $850\,\mu\text{m}$ data with *Herschel* SPIRE/PACS continuum observations. The average column density and temperature values for each clump are also derived.

(iii) The average volume density for each clump and region was computed. The values for regions R2 and R3 are $\sim 4.09 \times 10^4\,\text{cm}^{-3}$ and $4.71 \times 10^4\,\text{cm}^{-3}$, respectively.

(iv) The B-field morphology is random for C3 and C6, perpendicular for clumps C4 and C7, and parallel for C5, C8 and C9.

(v) In region R3, the B-field morphology at sub-pc scale may be linked to the large-scale field structure, as they appear to follow the same direction.

(vi) The magnetic field strength in region R2 is estimated to be 83.4 ± 10.3 µG using the SF analysis on the modified DCF method. For region R3, the field strength is 83.3 ± 15.7 µG, estimated using only the modified DCF method.

(vii) The regions R2 and R3 are magnetically subcritical with the λ value of 0.78 ± 0.15 and 0.58 ± 0.12, respectively, whereas L328 core is transcritical with the value of 1.1 ± 0.2.

(viii) All the regions are found to be sub-Alfvénic except C5 clump.

(ix) The polarization fraction as a function of total intensity is found to be decreasing in the high-density region, indicating depolarization in all the regions with a power-law slope of -0.97, -0.94, -0.91, and -0.98, respectively. Finally, if we combine all the regions, we still see a slope of -0.91.

DATA AVAILABILITY

The data used in this article will be shared on reasonable request to the corresponding author.

REFERENCES

Andersson B. G., Lazarian A., Vaillancourt J. E., 2015, ARA&A, 53, 501

Astropy Collaboration, 2013, A&A, 558, A33

Astropy Collaboration, 2018, AJ, 156, 123

Astropy Collaboration, 2022, ApJ, 935, 167

Bate M. R., Bonnell I. A., Bromm V., 2003, MNRAS, 339, 577

Beckwith S. V. W., Sargent A. I., Chini R. S., Guesten R., 1990, AJ, 99, 924

Berry D. S., 2015, Astron. Comput., 10, 22

Berry D. S., Reinhold K., Jenness T., Economou F., 2007, in Shaw R. A., Hill F., Bell D. J., eds, ASP Conf. Ser. Vol. 376, Astronomical Data Analysis Software and Systems XVI. Astron. Soc. Pac., San Francisco, p. 425

Chandrasekhar S., Fermi E., 1953, ApJ, 118, 113

Chapin E. L., Berry D. S., Gibb A. G., Jenness T., Scott D., Tilanus R. P. J., Economou F., Holland W. S., 2013, MNRAS, 430, 2545

Crutcher R. M., 2004, Ap&SS, 292, 225

Crutcher R. M., Troland T. H., Lazareff B., Paubert G., Kazès I., 1999, ApJ, 514, L121

Crutcher R. M., Nutter D. J., Ward-Thompson D., Kirk J. M., 2004, ApJ, 600, 279

Currie M. J., Berry D. S., Jenness T., Gibb A. G., Bell G. S., Draper P. W., 2014, in Manset N., Forshay P., eds, ASP Conf. Ser. Vol. 485, Astronomical Data Analysis Software and Systems XXIII. Astron. Soc. Pac., San Francisco, p. 391

Czesla S., Schröter S., Schneider C. P., Huber K. F., Pfeifer F., Andreasen D. T., Zechmeister M., 2019, Astrophysics Source Code Library, record ascl:1906.010

Davis L., 1951, Phys. Rev., 81, 890

Dolginov A. Z., Mitrofanov I. G., 1976, Ap&SS, 43, 291

Eden D. J. et al., 2017, MNRAS, 469, 2163

Eden D. J. et al., 2019, MNRAS, 485, 2895

Elia D. et al., 2017, MNRAS, 471, 100

Friberg P., Bastien P., Berry D., Savini G., Graves S. F., Pattle K., 2016, in Holland W. S., Zmuidzinas J., eds, Proc. SPIE Conf. Vol. 9914, Millimeter, Submillimeter, and Far-Infrared Detectors and Instrumentation for Astronomy VIII. SPIE, Bellingham, p. 991403

Gupta S., Soam A., Karoly J., Lee C. W., Maheswar G., 2025, MNRAS, 539, 3493

Hall J. S., 1949, Science, 109, 166

Harris C. R. et al., 2020, Nature, 585, 357

Hennebelle P., Chabrier G., 2008, ApJ, 684, 395

Hennebelle P., Inutsuka S.-i., 2019, Front. Astron. Space Sci., 6, 5

Hildebrand R. H., Kirby L., Dotson J. L., Houde M., Vaillancourt J. E., 2009, ApJ, 696, 567

Hiltner W. A., 1949, ApJ, 109, 471

Hoang T., Lazarian A., 2008, MNRAS, 388, 117

Holland W. S. et al., 2013, MNRAS, 430, 2513

Kauffmann J., Bertoldi F., Bourke T. L., Evans N. J., II, Lee C. W., 2008, A&A, 487, 993

Kumar S., Soam A., Roy N., 2023, MNRAS, 524, 1219

Lada C. J., Lada E. A., 2003, ARA&A, 41, 57

Lazarian A., 2007, J. Quant. Spectrosc. Radiat. Transf., 106, 225

Lazarian A., Hoang T., 2007, MNRAS, 378, 910

Lazarian A., Vishniac E. T., 1999, ApJ, 517, 700

Lee C. W. et al., 2018, ApJ, 865, 131

Mairs S. et al., 2021, AJ, 162, 191

Montier L., Plaszczynski S., Levrier F., Tristram M., Alina D., Ristorcelli I., Bernard J. P., Guillet V., 2015, A&A, 574, A136

Ostriker E. C., Stone J. M., Gammie C. F., 2001, ApJ, 546, 980

Pattle K., Fissel L., Tahani M., Liu T., Ntormousi E., 2023, in Inutsuka S.-i., Aikawa Y., Muto T., Tomida K., Tamura M., eds, ASP Conf. Ser. Vol. 534, Protostars and Planets VII. Astron. Soc. Pac., San Francisco, p. 193

Planck Collaboration XXXV, 2016a, A&A, 586, A138

Planck Collaboration I, 2016b, A&A, 594, A1

Planck Collaboration XXVI, 2016c, A&A, 594, A26

Plaszczynski S., Montier L., Levrier F., Tristram M., 2014, MNRAS, 439, 4048

Robitaille T., 2019, APLpy v2.0: The Astronomical Plotting Library in Python. Zenodo. https://doi.org/10.5281/zenodo.2567476

Robitaille T., Bressert E., 2012, Astrophysics Source Code Library, record ascl:1208.017

Soam A., Maheswar G., Bhatt H. C., Lee C. W., Ramaprakash A. N., 2013, MNRAS, 432, 1502

Soam A., Maheswar G., Lee C. W., Dib S., Bhatt H. C., Tamura M., Kim G., 2015a, A&A, 573, A34

Soam A., Kwon J., Maheswar G., Tamura M., Lee C. W., 2015b, ApJ, 803, L20

Soam A., Andersson B. G., Acosta-Pulido J., Fernández López M., Vaillancourt J. E., Widicus Weaver S. L., Piirola V., Gordon M. S., 2021, ApJ, 907, 93

Soam A., Eswaraiah C., Seta A., Dewangan L., Maheswar G., 2024, J. Astrophys. Astron., 45, 17

Urquhart J. S. et al., 2018, MNRAS, 473, 1059

Veltchev T. V., Donkov S., Klessen R. S., 2013, MNRAS, 432, 3495

Virtanen P. et al., 2020, Nat. Methods, 17, 261

Wu J., Dunham M. M., Evans N. J., II, Bourke T. L., Young C. H., 2007, AJ, 133, 1560

This paper has been typeset from a TeX/LaTeX file prepared by the author.